



Two novel titanium alloys for medical applications: Thermo-mechanical treatment, mechanical properties, and fracture analysis

Fabian Haase^{1,a)}, Carsten Siemers¹, Joachim Rösler¹

¹ Technische Universität Braunschweig, Institute for Materials Science, Langer Kamp 8, Braunschweig 38106, Germany

^{a)} Address all correspondence to this author. e-mail: f.haase@tu-braunschweig.de

Received: 21 February 2022; accepted: 17 May 2022; published online: 2 June 2022

Titanium alloys are ideally suited for use in implant or osteosynthesis applications due to their good mechanical properties, corrosion resistance, and biocompatibility. In terms of higher strength applications, Ti-6Al-4V and Ti-6Al-7Nb are frequently used. However, both alloys contain the alloying elements aluminum and, in the former case, vanadium, which could have toxic effects on the human body. Therefore, in the present study, two novel, medium- to high-strength titanium alloys, Ti-0.44O-0.5Fe-0.08C-0.4Si-0.1Au and Ti-0.44O-0.5Fe-0.08C-2.0Mo, have been developed on the basis of CP-Titanium Grade 4. They only contain alloying elements, which are either already present in the human body or which are biocompatible. Dedicated thermo-mechanical treatments were developed for both alloys and the resulting mechanical properties were evaluated by tensile and (partly) fatigue tests with subsequent fracture surface analysis. Results reveal that these new alloys show excellent mechanical properties and, therefore, might be a possible alternative for Ti-6Al-4V for use in medical applications.

Introduction

Several materials are used in medical engineering, but titanium and titanium alloys are the best suited due to their combination of good mechanical properties, corrosion resistance, and biocompatibility [1, 2]. In terms of α and $(\alpha + \beta)$ alloys, CP-Titanium (lower strength applications) and Ti-6Al-4V (either as standard alloy or with extra low interstitials, Ti-6Al-4V ELI), Ti-6Al-7Nb or Ti-5Al-2.5Fe (higher strength applications) are often used [1, 2]. Since vanadium is a toxic element, which might also have a toxic effect on the human body when used as alloying element in implant materials, the latter two alloys were developed as alternative for Ti-6Al-4V and contain niobium and iron, respectively, instead of vanadium [1, 2]. However, those $(\alpha + \beta)$ alloys still contain aluminum as alloying element, whose proven and suspected detrimental effects on the human health have been intensively studied regarding several aspects of daily life. On the one hand, aluminum can be neurotoxic [3–6]. This neurotoxicity has been linked with several effects on the human body or diseases, including dementia [3, 6]. On the other hand, a possible relationship between aluminum and, among others, Alzheimer's disease has been investigated and discussed

in several publications [3–7]. Due to possible detrimental effects of occupational or non-occupational aluminum exposure, associated health risks have been assessed comprehensively, for example in the studies by Tietz et al. [5] or Krewski et al. [7].

As far as the authors know, no detrimental effects on human health due to use of aluminum-containing titanium alloys as implant material have been reported so far. However, since adverse effects might be possible, the development of titanium alloys which contain a non-critical substitute for the alloying element aluminum (as done with vanadium in the past) would be of benefit to patients. Moreover, the patient acceptance of such an alloy might be higher compared to conventional, aluminum-containing titanium alloys, since the general population becomes sensitized regarding aluminum exposure.

Therefore, in the present study, two medium- to high-strength titanium alloys, Ti-0.44O-0.5Fe-0.08C-0.4Si-0.1Au and Ti-0.44O-0.5Fe-0.08C-2.0Mo, were developed as possible alternatives for Ti-6Al-4V. Both were produced in larger scale, which, in terms of the molybdenum containing alloy, resulted in a slightly different chemical composition of Ti-0.63O-0.58Fe-0.096C-2.10Mo. First, several

thermo-mechanical processing routes for plate rolling had been studied in terms of Ti-0.44O-0.5Fe-0.08C-0.4Si-0.1Au in order to achieve a fine-grained equiaxed microstructure after recrystallization annealing with low amounts of retained lamellae. The resulting, optimized multi-step processing route is described in detail in the present study together with the microstructure evolution after the different steps of this route. Afterward, additional studies were performed on Ti-0.44O-0.5Fe-0.08C-2.0Mo (regarding an additional lot, produced in larger scale, but with slightly lower molybdenum content). Since comparable findings were found, the optimized processing route of Ti-0.44O-0.5Fe-0.08C-0.4Si-0.1Au was adapted to Ti-0.63O-0.58Fe-0.096C-2.10Mo. This adapted route, the microstructures obtained, and differences to Ti-0.44O-0.5Fe-0.08C-0.4Si-0.1Au are also described in detail in the present study. Additionally, tensile tests with subsequent fracture analysis were performed on both alloys. In terms of Ti-0.44O-0.5Fe-0.08C-0.4Si-0.1Au, these tests have been performed regarding two rolled plates with different thicknesses, since a different plate thickness during one vital step of the processing route influenced the resulting microstructure and, hence, the mechanical properties. Additionally, tensile tests as well as fatigue tests with subsequent fracture analyses were performed at rotary swaged rods of this alloy in the recrystallized state. Ti-0.44O-0.5Fe-0.08C-2.0Mo (produced in laboratory scale) and Ti-0.44O-0.5Fe-0.08C-0.4Si-0.1Au have already been (briefly) addressed elsewhere [8].

Both alloys are based on CP-Titanium Grade 4+ (which is Titanium Grade 4 with maximum allowed content of oxygen, iron, and carbon according to ASTM F67-13 [9]; Ti-0.4O-0.5Fe-0.08C) and several other in-house alloy developments for use in medical applications [10, 11]. In terms of the chemical composition of the alloys discussed in the present study, oxygen and carbon are central elements of the human body, iron and molybdenum are essential (trace) elements, and silicon is under consideration to be classified as essential [12]. Gold is not a required (trace) element [12], but is seen as biocompatible [2]. However, it has to be noted that, on the one hand, the classification of elements as essential/non-essential/

detrimental might change over time due to ongoing research, and, on the other hand, the doses of a particular element in the human body has an influence, whether it has a detrimental or—in case of essential elements—beneficial effect [12]. As a consequence of this, CP-Titanium was used as basis for alloy development to ensure high corrosion resistance (low amount of ions released in surrounding tissue), and only low amounts of alloying elements were added for solid solution strengthening. Therefore, it is expected that both alloys show an improved biocompatibility compared to Ti-6Al-4V.

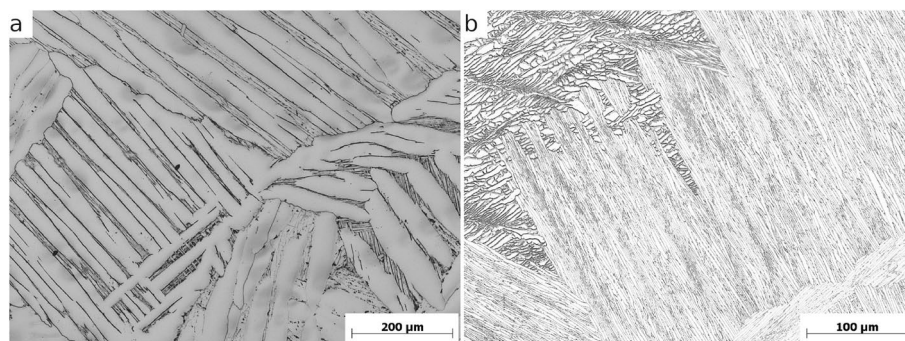
The microstructure evolution described in this study is solely related to thermo-mechanical processing in order to obtain a wrought material with a suitable microstructure for subsequent fabrication of final parts. However, welding might be performed on semi-finished products leading to a heat affected zone alongside of the weld pool and, consequently, to changes in microstructure and mechanical properties either after welding or during post weld heat treatments [13]. The microstructure evolution within such heat affected zones is beyond the scope of the present study, although being relevant for the application of finished products and although several findings of the present investigation may apply as well. The reader may consult for instance the study by Akhtar et al. [14] and Khajuria et al. [15] to get an overview how different subzones of heat effected zones can be simulated experimentally, analyzed, and characterized in terms of for example phase transformations, the role of alloying elements, and mechanical properties. Some of these procedures are also applicable for optimizing thermo-mechanical treatments.

Results and discussion

Microstructure evolution

Figure 1 shows the microstructure of Ti-0.44O-0.5Fe-0.08C-0.4Si-0.1Au (a) and Ti-0.63O-0.58Fe-0.096C-2.10Mo (b) in the as received condition. Ti-0.44O-0.5Fe-0.08C-0.4Si-0.1Au exhibits a coarse bi-lamellar microstructure with primary α -laths, fine secondary α -laths with widths up to a few micrometers formed in former β -laths, and grain-boundary- α . Partly,

Figure 1: Microstructure of Ti-0.44O-0.5Fe-0.08C-0.4Si-0.1Au (a) and Ti-0.63O-0.58Fe-0.096C-2.10Mo (b) in the as received condition.



irregular or massive α -structures are visible (not shown in the images). In terms of Ti–0.63O–0.58Fe–0.096C–2.10Mo, a different lamellar microstructure is present in the as received condition as can be seen in Fig. 1(b): Individual α -lamellae exhibit a width of only a few micrometers, but, partly, form α -colonies with widths up to several hundred micrometers. However, many laths have an irregular shape and differ significantly in length and width. As a result, the laths do not exhibit the typical elongated, straight, and parallel geometry (within colonies). These laths and colonies, therefore, differ from those typically observed in lamellar microstructures of titanium alloys. Moreover, irregular or massive, partly equiaxed α -grains, as can be seen in the top left corner of Fig. 1(b), and grain-boundary- α are present. In both microstructures, β -phase is present as evident by high-magnification SEM images, EDX analysis (enrichment of the β -stabilizers iron or molybdenum in β -grains), and XRD analysis.

After solution treatment close to β -transus with subsequent water quenching during the multi-step processing route (rolling), the microstructure of Ti–0.44O–0.5Fe–0.08C–0.4Si–0.1Au depends on plate thickness prior to annealing. This is depicted in Fig. 2, which shows the microstructure (cross section) in the center of a plate's cross section in terms of a plate thickness of approx. 8 mm (a) and approx. 12 mm (b). As can be seen, the thinner plate exhibits a martensitic microstructure throughout the cross section and some retained α -grains. The thicker plate, however, shows a lamellar microstructure with grain-boundary- α in the plate's center due to slower cooling. This particular plate, analyzed in the present study, showed martensite only within a very narrow surface layer in terms of the middle part of the plate. At the edge of the plate with regard to the plate's width, however, martensite was present over the full plate's thickness or in a much higher depth. Another similar processed plate (not covered by the present study) with comparable thickness before solution treatment (but with the thermal barrier coating still applied during solution treatment) exhibited the same microstructure, but martensite was present within a thicker surface layer. Additionally, the thickness of this martensitic layer varied in terms of the plate's width. This indicates that the cooling rate,

on the one hand, might not be homogeneous throughout the plate's profile during water quenching and, on the other hand, cannot be kept constant. However, the applied thermal barrier coating may have influenced these results. Moreover, the martensite present in both plates described in the present study exhibit an acicular as well as massive morphology. The latter is undesired, since parallel martensite plates decompose to α -colonies during subsequent annealing and do not always get broken down fully during final rolling. This leads to retained lamellae within the recrystallized microstructure as described later. Retained α -grains can be beneficial in order to limit β -gain growth and, thus, the size of α -colonies or of massive martensite.

Consequently, after subsequent annealing, the microstructure of the thicker plate is inhomogeneous with respect to the plate's cross section, since martensite decomposed during annealing, whereas existing lamellae became coarser. This is depicted in Fig. 3, which shows the microstructure (cross section) at the edge of the plate in terms of the plate's width (a) and in the center of the cross section (b). As can be seen in Fig. 3(a), acicular martensite fully decomposed to fine ($\alpha + \beta$) lamellae and α -colonies were formed out of massive martensite. In the center of the plate's cross section, however, the microstructure became much coarser and still consists of coarse α -colonies and grain-boundary- α , as seen in figure (b). For comparison, Fig. 4 depicts the microstructure of the thinner plate at similar locations of the plate's cross section. As evident, martensite decomposition and formation of fine lamellae (former acicular martensite) and α -colonies (former massive martensite) took place along the entire plate's width leading to a homogeneous microstructure.

As a result, there is no significant difference in the rolled and recrystallized microstructure across the width of the thinner plate, as can be seen in the upper half of Fig. 5, which shows the microstructure in longitudinal direction at the edge and in the middle of the plate in terms of the plate's width. The microstructure consists of fine, equiaxed α -grains, which are not fully homogeneous in size, and a comparable small amount of β -grains. However, there are also retained lamellae present, which were not broken down (fully) during rolling. In this case,

Figure 2: Microstructure of Ti–0.44O–0.5Fe–0.08C–0.4Si–0.1Au after solution treatment in the center of a plate's cross section regarding a plate thickness of approx. 8 mm (a) and of approx. 12 mm (b).

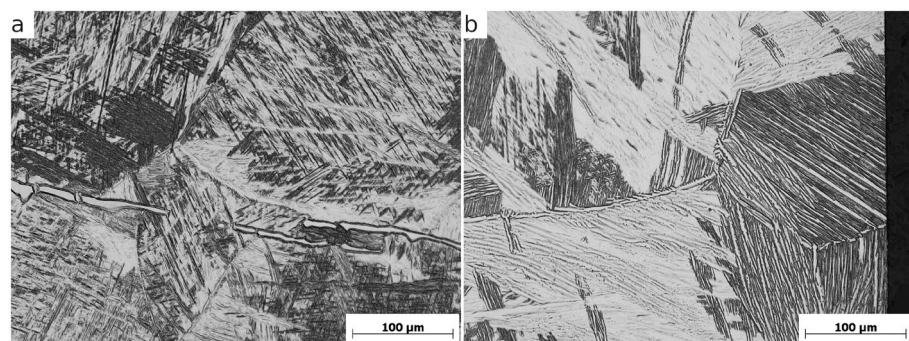


Figure 3: Microstructure of Ti-0.44O-0.5Fe-0.08C-0.4Si-0.1Au (thicker plate, cross section) after solution treatment and annealing at the edge of the plate in terms of the plate's width (a) and in the center of the cross section (b).

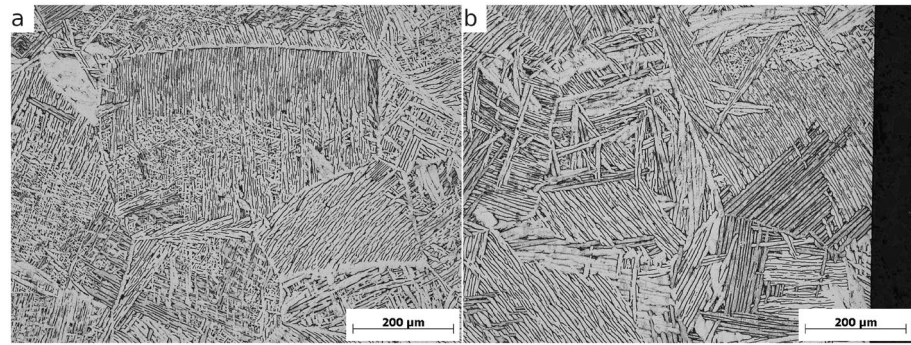


Figure 4: Microstructure of Ti-0.44O-0.5Fe-0.08C-0.4Si-0.1Au (thinner plate, cross section) after solution treatment and annealing at the edge of the plate in terms of the plate's width (a) and in the center of the cross section (b).

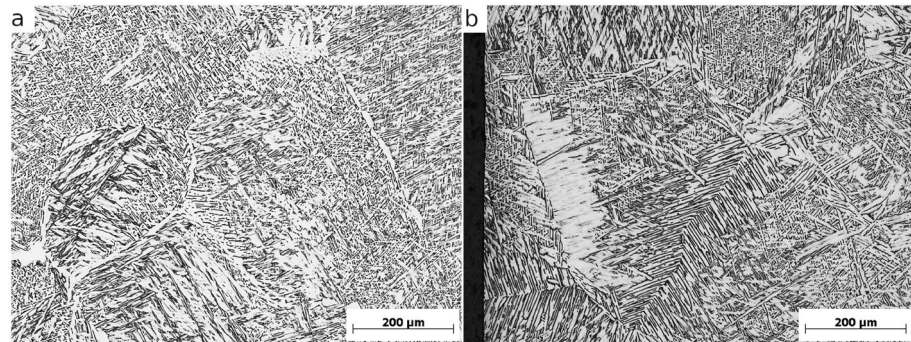
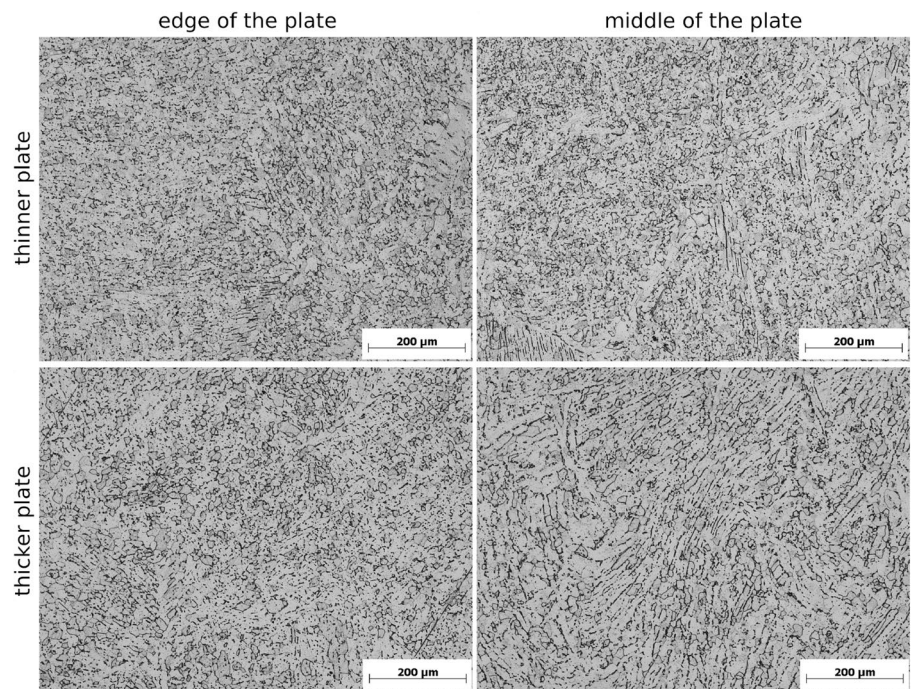


Figure 5: Comparison of the microstructure of Ti-0.44O-0.5Fe-0.08C-0.4Si-0.1Au (longitudinal section) at the edge and in the middle of the thinner and thicker plate in terms of the plate's width after final rolling and recrystallization annealing.



they have to result from decomposed massive martensite. In terms of the thicker plate, the microstructure at the edge of the plate in terms of the plate's width, see the lower left image of Fig. 5, where martensite was present after solution treatment, is finer, consisting primarily of recrystallized, equiaxed α -grains

(not homogeneous in size) and of a small amount of retained lamellae, compared to the middle of the plate, as shown in the lower right image of Fig. 5, where deformed but (mostly) unrecrystallized former α -colonies are still present in higher quantity. Consequently, the microstructure in the middle of the thicker

plate appears to be coarser compared to the thinner plate. Since the α -phase of (pure) titanium exhibits only a limited number of independent slip systems with close-packed slip directions [13], it is believed that the main reason for the presence of retained lamellae is the comparable low number of slip systems, which become activated in these lamellae during rolling. As a consequence, some lamellae remain (mostly) undeformed and are present in different sizes and with different degrees of recrystallization. Sometimes, pronounced plastic deformation or shearing of α -lamellae only took place within very narrow regions of α -colonies, indicating the presence of slip bands. As a result, equiaxed α -grains are formed within these slip bands only.

During subsequent studies on suitable thermo-mechanical processing routes in terms of Ti-0.44O-0.5Fe-0.08C-2.0Mo, it was found out that the same findings regarding the breakup and recrystallization of α -colonies mostly also apply to the molybdenum containing alloy. As a consequence, the processing route established for Ti-0.44O-0.5Fe-0.08C-0.4Si-0.1Au was adapted to Ti-0.63O-0.58Fe-0.096C-2.10Mo. In this case, only the solution annealing temperature had to be adjusted due to differences in β -transus of the alloys (the holding time has to be chosen with respect to plate thickness). Nevertheless, there are significant differences between the microstructures of both alloys during processing, which are described in the following.

After solution treatment close to β -transus of a plate with a thickness of approx. 12 mm, martensite was, in contrast to Ti-0.44O-0.5Fe-0.08C-0.4Si-0.1Au with same plate thickness, present throughout the entire cross section together with some

retained α -grains. The difference is attributed to the alloying element molybdenum which diffuses more slowly than the other alloying elements present here (see, for example, the study of Iijima et al. [16] for the diffusion of silicon and the study of Nakajima and Koiwa [17] for the diffusion of molybdenum in β -Ti), so that diffusion controlled transformation is retarded and martensitic transformation extended toward lower cooling rates. Martensite plates closer to the plate's surface had a different morphology with a much higher length. Since the size of the former β -grains is similar, this might be caused due to differences in cooling rate. After subsequent annealing, the martensite decomposed to a fine ($\alpha + \beta$)-microstructure as presented in Fig. 6 for the edge of the plate in terms of the plate's width (a) and the middle of the cross section (b). As can be seen, the microstructure is quite heterogeneous consisting, on the one hand, of primary α -lamellae with different lengths and widths due to differences in martensite, structures similar to α -colonies, and grain-boundary- α . On the other hand, (almost) equiaxed α -grains and fine secondary α -lamellae formed in (prior) β -lamellae or grains are present, which both indicates that the amount of β -phase was comparable high during annealing, thus leading to a bi-lamellar microstructure after air cooling.

After final rolling and recrystallization annealing, equiaxed α -grains, retained (deformed) α -lamellae and α -colonies, grain-boundary- α as well as β -grains are present, as can be seen in Fig. 7, which shows an optical microscopy micrograph in the middle of the plate in terms of the plate's width (a) and a SEM image (b). Since a BSE detector was used, β -grains

Figure 6: Microstructure of Ti-0.63O-0.58Fe-0.096C-2.10Mo (cross section) after solution treatment and annealing at the edge of the plate in terms of the plate's width (a) and in the middle of the cross section (b).

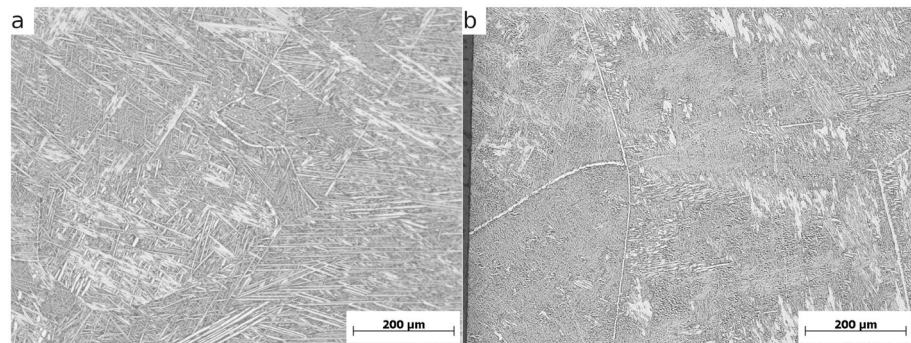
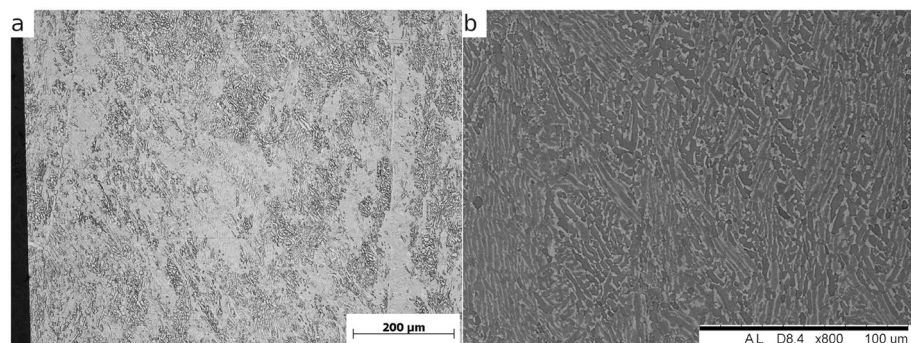


Figure 7: Microstructure of Ti-0.63O-0.58Fe-0.096C-2.10Mo (longitudinal section) after final rolling and recrystallization annealing: (a) optical microscopy micrograph, middle of the plate in terms of the plate's width, (b) SEM image using a BSE detector.



are clearly distinguishable from α -grains, since the alloying element molybdenum, as a β -stabilizer, partitions into the β -phase [13], thus leading to a higher mass contrast. In comparison with the thinner and thicker plate of Ti-0.44O-0.5Fe-0.08C-0.4Si-0.1Au, see Fig. 5, the number of retained lamellae is comparable high. However, the microstructure is much finer as can be seen in Fig. 7(b): Very fine equiaxed or elongated α - as well as β -grains in the nanometer- and micrometer-range are present.

To summarize microstructure evolution during thermo-mechanical processing (rolling) of both alloys, it can be concluded that a fine lamellar ($\alpha + \beta$) microstructure obtained via full martensite decomposition is an ideal initial microstructure for final rolling: Fine recrystallized, equiaxed α -grains with (compared to, for example, full lamellar microstructures obtained via air cooling after annealing close to/above β -transus) small amounts of retained lamellae are obtainable. However, in case of thicker plates of Ti-0.44O-0.5Fe-0.08C-0.4Si-0.1Au, a martensitic microstructure cannot be obtained throughout the entire plate, leading to a higher amount of unrecrystallized lamellae. In general, such retained α -colonies indicate that the degree of deformation during final rolling was not sufficient enough for a full breakdown of the microstructure. This deformation degree was limited in this study due to processing under laboratory conditions, since final rolling had to be performed with a thickness reduction of only approx. 0.2 mm during each pass and with subsequent annealing prior to further rolling. Consequently, during industrial thermo-mechanical processing, a better microstructure should be obtainable for both alloys after recrystallization annealing.

In terms of Ti-0.44O-0.5Fe-0.08C-0.4Si-0.1Au, rods of this alloy were also rotary swaged and recrystallization annealed. In general, the microstructures (longitudinal sections) of the recrystallized rods are coarser compared to rolled plates, although the same recrystallization annealing treatment was performed. This indicates that the “effective” degree of deformation—that is the total degree of deformation less the deformation degree lost for recrystallization due to recovery of the microstructure—was lower than after rolling. Moreover, to some extent, different rods exhibit a different microstructure, and, furthermore, this structure is not homogeneous along the longitudinal axis as well as along the thickness of rods. In terms of the edge area of rods and longitudinal sections, equiaxed α -grains are present (almost) exclusively, with the exception of one analyzed rod, which also exhibited retained lamellae to some extent. However, in terms of the center of the rods, equiaxed primary α as well as elongated α -grains or retained lamellae are present. The extent of which elongated grains or retained lamellae are present differs along the longitudinal axis as well as between rods. Additionally, β -grains are present.

Mechanical properties

Table 1 lists the mechanical properties of Ti-0.44O-0.5Fe-0.08C-0.4Si-0.1Au and Ti-0.63O-0.58Fe-0.096C-2.10Mo after rolling or rotary swaging and recrystallization annealing in terms of the yield strength, YTS, ultimate tensile strength, UTS, and the elongation after fracture, A. Additionally, minimum requirements and typical values of Ti-6Al-4V are listed for comparison. In terms of Ti-0.44O-0.5Fe-0.08C-0.4Si-0.1Au, the rotary swaged and recrystallized material exhibits the highest yield and ultimate tensile strength, which are within typical values of Ti-6Al-4V. In contrast, the elongation after fracture is lower compared to rolled material of this alloy, but is still higher than typical elongations of Ti-6Al-4V. However, it has to be noted that the rupture elongation is stated for one of two tested tensile specimens only, since it is expected that this value is representative. The other specimen fractured prematurely at an elongation of 10.5% with fracture analysis suggesting the presence of a manufacturing defect. In terms of rolled material of this alloy, it can be seen that the thickness prior to solution annealing has an impact on mechanical properties. The thinner plate exhibits a yield and ultimate tensile strength of approx. 850 MPa and approx. 890 MPa, respectively, which are (almost) within typical values of Ti-6Al-4V, but at least higher than minimum requirements. The thicker plate, however, exhibits a yield and ultimate tensile strength of approx. 825 MPa and approx. 835 MPa, respectively, and, consequently, lower mechanical properties, which do not fulfill minimum requirements of Ti-6Al-4V (in regard to UTS). The elongation

TABLE 1: Mechanical properties (mean values if not indicated otherwise) of the studied alloys and required and typical values of Ti-6Al-4V.

Alloy	YTS (MPa)	UTS (MPa)	A (%)
Ti-0.44O-0.5Fe-0.08C-0.4Si-0.1Au	872 ^a	910 ^a	18.3 ^{a,b}
	851 ^{c,d}	892 ^{c,d}	21.6 ^{c,d}
	826 ^{c,e}	836 ^{c,e}	22.1 ^{b,c,e}
Ti-0.63O-0.58Fe-0.096C-2.10Mo	1116 ^c	1153 ^{c,f}	16.5 ^c
Ti-6Al-4V	780 ^g	860 ^g	10 ^g
	800-1100 ^h	900-1200 ^h	13-16 ^h

^aRotary swaged and recrystallized material.

^bValue representative/valid specimen.

^cRolled and recrystallized material.

^dThinner plate (prior to solution annealing).

^eThicker plate (prior to solution annealing).

^fPossibly overestimated by up to 11 MPa.

^gMinimum requirements for rods according to DIN EN ISO 5832-3:2017-03 [18].

^hTypical values [19].

after fracture, however, is similar for both plates and, additionally, much higher than typical values of Ti-6Al-4V. In terms of the thicker plate, the elongation after fracture is stated for one tested tensile specimen only, since, regarding the second specimen, rupture probably occurred outside of the measurement section, therefore, leading to an underestimated rupture elongation of approx. 3%.

As already described, the difference between the rotary swaged and rolled specimens (thinner plate) of Ti-0.44O-0.5Fe-0.08C-0.4Si-0.1Au is in particular the coarser microstructure of the rotary swaged material. According to basic principles of grain-boundary strengthening, the rotary swaged material should therefore exhibit a lower yield and ultimate tensile strength compared to the rolled material. However, the opposite is the case. On the one hand, differences in texture might exist, since both deformation processes differ in material flow and since the deformation temperature was different. In terms of unidirectional rolling and ($\alpha + \beta$)-alloys, it is already established that the deformation temperature has an influence on, among others, texture intensity [13]. Due to the overall poorer deformability of the α -phase [13], the slip systems might be more unfavorably oriented in the rotary swaged material during tensile testing compared to the rolled specimens, so that their activation is more difficult. This might also explain the significant lower ductility. On the other hand, the rotary swaged material might exhibit a higher amount of retained work hardening due to a poorer recrystallization of the microstructure, therefore, leading to a higher yield strength and lower ductility. However, the ratio between yield and ultimate tensile strength is similar for the rotary swaged material and the thinner plate of the rolled material, therefore, suggesting a comparable amount, if any, of retained work hardening.

Regarding the rolled material of Ti-0.44O-0.5Fe-0.08C-0.4Si-0.1Au, the higher yield and ultimate tensile strength of the thinner plate could be attributed to its overall finer and more homogeneous microstructure after recrystallization annealing. This is the result of the homogeneous and finer microstructure of the thinner plate after solution treatment and annealing, consisting of decomposed martensite throughout the cross section, which enhances microstructure breakup during subsequent rolling and formation of equiaxed grains, as already described. This conclusion can be made even if the thicker plate did not exhibit the same degree of deformation (approx. 0.80) during final rolling than the thinner plate (approx. 0.71), since a higher deformation degree tends to increase microstructure breakup, therefore, promoting recrystallization and the formation of a finer microstructure with enhanced mechanical properties. As described above, major differences between the recrystallized microstructures of both plates are the larger amount of deformed, mostly unrecrystallized former α -colonies present in the middle of the thicker plate and its coarser microstructure

compared to the thinner plate. With regard to grain-boundary hardening, the lower yield and ultimate tensile strengths of the thicker plate might be the result of these microstructural differences. Moreover, the higher yield ratio of the thicker plate of approx. 99% compared to approx. 95% of the thinner plate might suggest that the thicker plate exhibits a greater amount of retained work hardening, which might be a result of the larger quantity of (mostly) unrecrystallized α -colonies present in related specimens. However, the presence of retained work hardening would be inconsistent to the similar elongation after fracture as well as to the greater uniform plastic elongation of the thicker plate of approx. 10% (representative specimen only) compared to an uniform plastic elongation of approx. 8% of the thinner plate, though this might also be the result of the limited number of specimens tested in terms of the thicker plate.

Ti-0.63O-0.58Fe-0.096C-2.10Mo exhibits a very high yield and ultimate tensile strength of 1116 MPa and approx. 1153 MPa, respectively, combined with an elongation after fracture of 16.5%. However, it has to be noted that the ultimate tensile strength might be overestimated by up to 11 MPa due to use of a hysteresis loop during testing for better determination of the elastic modulus (and, thus, yield strength). It is usually observed that the stress after performing the hysteresis loop increases beyond the stress value measured before. As a consequence, this behavior might have influenced UTS determination, since the loop was performed close to UTS of this alloy. As stated in Table 1, Ti-6Al-4V can reach such high static mechanical properties, but as far as the authors know, those values are only obtainable when multi-step annealing treatments for microstructural optimization are applied. In contrast, Ti-0.63O-0.58Fe-0.096C-2.10Mo exhibits such values after applying a standard recrystallization treatment for obtaining an equiaxed microstructure.

The much higher strength of Ti-0.63O-0.58Fe-0.096C-2.10Mo compared to Ti-0.44O-0.5Fe-0.08C-0.4Si-0.1Au is assumed to be the result of a significant higher solid solution strengthening as well as of the much finer microstructure (grain-boundary hardening) of the molybdenum containing alloy. Earlier investigations with, among others, the alloy systems Ti-0.44O-0.5Fe-0.08C-0.4Si and Ti-0.44O-0.5Fe-0.08C-2.0Mo regarding laboratory-size specimens already revealed a higher yield and ultimate tensile strength of the latter alloy as well as a strong solid solution strengthening effect of the alloying element oxygen [8]. Consequently, due to the much higher oxygen content in Ti-0.63O-0.58Fe-0.096C-2.10Mo compared to Ti-0.44O-0.5Fe-0.08C-0.4Si-0.1Au, it is believed that this alloying element strongly contributes to the much higher strength. This solid solution strengthening effect could also be responsible for the lower ductility of the molybdenum containing alloy despite of the finer microstructure. Additionally, it is expected that the higher amount of β -phase in the molybdenum containing

alloy has a positive effect on the strength, because the number of phase- or grain-boundaries is increased [8]. Since retained lamellae are present to a higher extent, a certain amount of retained work hardening compared to the thinner plate of Ti-0.44O-0.5Fe-0.08C-0.4Si-0.1Au would be expected according to the previous statements. This is reasonable to accept, since the yield ratio is at least approx. 97% due to the possible overestimation of the ultimate tensile strength. This work hardening would lead to an increased yield strength and a decreased ductility.

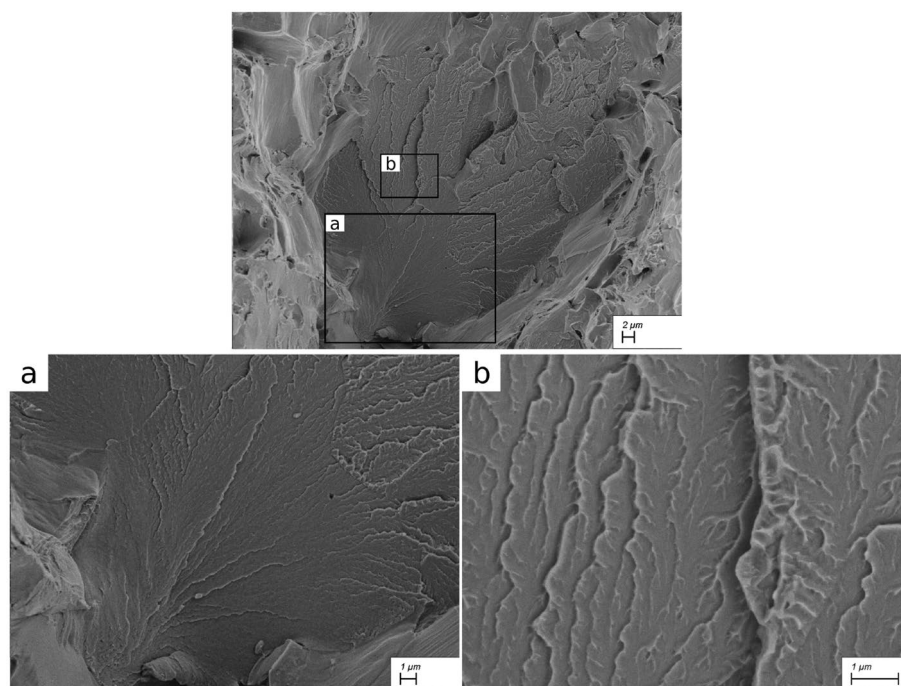
In terms of fatigue tests regarding rotary swaged and recrystallized material of Ti-0.44O-0.5Fe-0.08C-0.4Si-0.1Au, fracture of fatigue specimens occurred at a stress amplitude of approx. 298 MPa ($R \approx 0.02$) and 270 MPa ($R \approx 0.03$). One specimen failed after only approx. 591,000 cycles with a stress amplitude of approx. 247 MPa ($R \approx 0.02$). However, fracture surface analysis revealed the presence of a retained radial score mark, which is adjacent to the fracture surface. Therefore, it was concluded that this score mark acted as notch leading to stress concentrations and, thus, promoting early fatigue failure. A second specimen tested with a stress amplitude of approx. 248 MPa and a R-value of approx. 0.02 did not fail (5×10^6 cycles), as well as a specimen tested with a stress amplitude of approx. 266 MPa and a R-value of approx. 0.04. Although the number of tests performed is not sufficient for a reliable statement regarding fatigue properties, it indicates that the fatigue endurance limit is higher compared to Ti-6Al-4V ELI. Ono et al. [20] performed high cycle fatigue tests on Ti-6Al-4V ELI under similar conditions as in the present study (microstructure with equiaxed primary α -grains, fatigue tests with a stress ratio R of 0.01, a frequency

of 10–15 Hz, and a temperature of 293K) with up to 10^7 cycles instead of 5×10^6 cycles of the present study. A stress amplitude of approx. 200 MPa and of approx. 150 MPa was withstood for approx. 10^6 and 10^7 cycles, respectively [20]. This is much less than the stress levels used in the present study.

Fracture surface analysis

All mechanical experiments were accompanied by fracture surface analysis to determine the microscopic fracture behavior. Since both alloys contain a higher amount of oxygen, they might be prone to fracture via a microscopic brittle mechanism [13], which would, possibly, limit the usability of the alloys. In terms of tensile specimens, the fracture surfaces predominantly show dimples regardless of processing via rolling or rotary swaging. These dimples are characteristic for a microscopic ductile fracture [21]. Additionally, features as depicted in Fig. 8 (fracture surface of Ti-0.44O-0.5Fe-0.08C-0.4Si-0.1Au; rotary swaged and recrystallized material) are present locally, which will be designated as “facets”. Facets are often seen in terms of titanium alloys [22]. In case of the present study, these facets exhibit different appearances, which are shown in the detail images (a) and (b) of Fig. 8. To a minor extent, facets exhibit (only) river patterns as seen in image (a), which are characteristics of a transgranular cleavage fracture [23]. In this case, it can be seen that the crack originates somewhere near the bottom left corner and propagates to the upper right. In the direction of crack propagation there are, first, several steps or river patterns. However, several ridges appear in crack propagation direction,

Figure 8: Fracture surface of Ti-0.44O-0.5Fe-0.08C-0.4Si-0.1Au (round tensile specimen, rotary swaged, and recrystallized material) showing facets with river patterns (a) and ductile ridges (b).



as can be seen in the upper right corner of Fig. 8(a). The high-resolution image (b) indicates that these features do not show the characteristic sharp edge of river patterns and rather seem to be the result of a much more ductile plastic flow of the material. Facets exhibiting these ridges are seen to a much higher extent compared to facets showing just/also river patterns. The ridges themselves can have a pronounced or weak appearance. All in all, their appearance is similar to those described in the literature (for example by Pilchak and Williams [22], who refer to several other studies regarding the influence of hydrogen and the appearance of facets in order to discuss their observations). To summarize, within their studies, Pilchak and Williams [22] connected the occurrence of these fracture surface features with the influence of hydrogen present in the alloy. Consequently, hydrogen might also have an influence regarding the alloys of the present study. However, since there is no clear evidence for this theory, it remains to be an assumption. In terms of the analyzed specimen of Ti-0.63O-0.58Fe-0.096C-2.10Mo, one crack initiation and propagation with the formation of steps and ductile ridges occurred on the shear lip. It is, therefore, more likely that this crack initiation occurred in the vicinity of the main crack during crack propagation. As a consequence, such facets do not necessarily appear to be initiation sites for main cracks and, therefore, to induce early specimen failure. Moreover, facets are only present locally with sizes of up to several ten micrometers, as can be seen in Fig. 8. Consequently, there is an overall much higher amount of dimples, which indicate good microscopic ductility.

In terms of fatigue tests, fracture surface analysis (fatigue and transient area only) was performed on the specimen tested at the highest stress amplitude of approx. 298 MPa (approx. 1,097,000 cycles, R-value approx. 0.02). One smaller part of the fracture surface fractured at a different location of the measuring section resulting in a distinct height change of the fracture surface. Since facets and striations are visible in both areas, it might be the case that two separate fatigue cracks were initiated and propagated through the material. In general, fatigue cracks are usually initiated as a surface crack and propagate via the formation of facets, i.e., crystallographic, and then via the formation of striations [22, 24]. Corrosive effects should, therefore, play a role during crystallographic propagation [24]. Additionally, it is established that laboratory air already has a negative effect on fatigue properties due to the influence of hydrogen [25].

In terms of the present study, the fracture surface might indicate an influence of hydrogen and the alloying element oxygen on the fatigue crack initiation or propagation. Figure 9 depicts an overview of the fracture surface as well as higher magnification images of two different locations (a) and (b). Location (a) is close to the height change and exhibits one facet with (almost) no visible roughness and other smooth facets. Since the former is characteristic for the initiation point of a

fatigue crack and the latter are characteristic for a small crack length [22], site (a) might be the crack initiation site or at least very close to it. This indicates that the corresponding fatigue crack was not formed as surface crack. In general, a high amount (much higher compared to the tensile specimens) of facets is present in the fatigue as well as in the transient area of the fracture surface. This already becomes apparent in the overview of the fracture surface in Fig. 9 and is further discussed in terms of site (b), which is close to the area of overload fracture. Facets with high roughness as well as striations are visible. The high-magnification image (c) shows that the fatigue crack propagates from the bottom left with the formation of facets. In propagation direction, a transition from facets to striations is visible, see arrow (d). These striations were formed over a short length of several micrometers only. The distance between individual striations is thereby small, which indicates an early stage of crack propagation [24]. However, at arrows (e) and (f), a punctiform source for crack propagation via the formation of facets seems to exist. These facets are very rough, which indicates that an existing crack with significant length propagated [22]. However, at arrow (g), striations are again visible. The reverse transition from facets to striations back to facets is also seen in Fig. 9(b). It, therefore, appears that the fatigue crack can change its way of propagation. This is unusual, since, as already described, there usually is a transition from crystallographic propagation to a ductile propagation with formation of striations [22, 24]. Moreover, ductile ridges are seen on some facets similar to those present in terms of the tensile specimens. However, Pilchak and Williams [22] did not observe these ridges regarding a continuously cycled specimen as in the present study, but only regarding dwell fatigue and tensile specimens. Since these ridges were connected with the influence of hydrogen [22], the results of the present study indicate that hydrogen might also have an influence on fatigue behavior in the alloy and fatigue tests studied here. This is consistent with the known negative influence of hydrogen on fatigue properties [25]. Additionally, on the one hand, it is established that the alloying element oxygen tends to lead to embrittlement [13]. On the other hand, a negative effect of oxygen on fatigue endurance limit was already reported by Amherd Hidalgo et al. [26], who produced Ti-6Al-7Nb via metal injection molding and with varying oxygen content. They suggested that this negative influence might be caused due to local embrittlement preventing stress concentration reduction [26]. These findings in the literature, the overall high amount of oxygen present in the alloy compared to conventional titanium alloys, the unusual changes in crack propagation, and the crack initiation within the specimen suggest, that the alloying element oxygen might have an impact on fatigue crack initiation or propagation in terms of the alloys studied here.

Despite of these findings, the mechanical properties of Ti-0.44O-0.5Fe-0.08C-0.4Si-0.1Au are (still) high. However, the

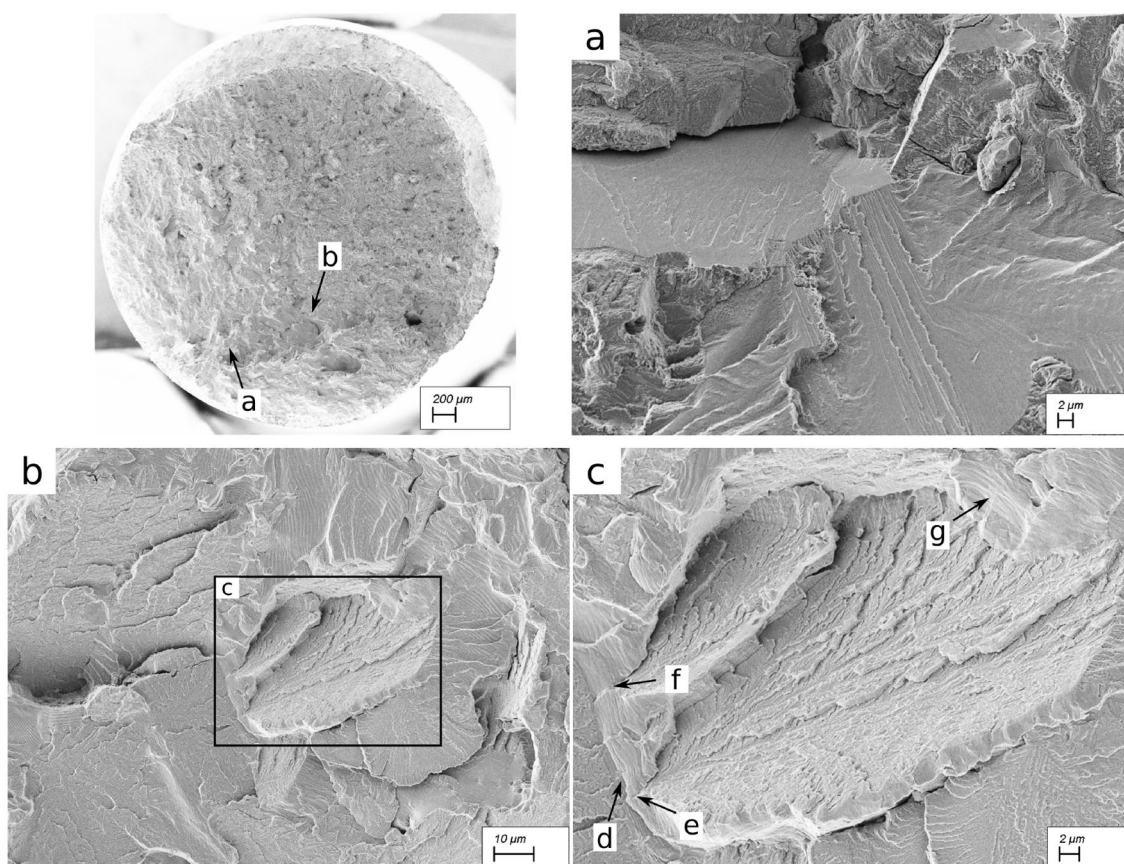


Figure 9: Fracture surface of a fatigue specimen (Ti-0.44O-0.5Fe-0.08C-0.4Si-0.1Au) at different locations (a), (b), and (c) of the surface. Arrows (d) and (g) show striations, whereas arrows (e) and (f) show a punctiform source for crack propagation via formation of facets.

number of performed fatigue tests is too small for a generalized statement. Although the precise influence or effect of oxygen and hydrogen remains unknown in the present study, it is expected that Ti-0.44O-0.5Fe-0.08C-0.4Si-0.1Au has a lower fatigue strength when used as implant material due to continual corrosive attacks in the human body.

Conclusion

In the present study, two novel titanium alloys, Ti-0.44O-0.5Fe-0.08C-0.4Si-0.1Au and Ti-0.63O-0.58Fe-0.096C-2.10Mo, for use in medical applications were developed and analyzed. First, a thermo-mechanical processing route for rolling under laboratory conditions was established and microstructure evolution during different stages of this processing route was described in detail for both alloys. Second, the resulting mechanical properties of rolled or rotary swaged and recrystallized material were examined via tensile and fatigue tests. Third, fracture surface analysis was performed to study the microscopic fracture behavior. The following conclusions can be drawn based on the results described:

- The developed multi-stage processing route for both alloys uses a full martensite decomposition prior to final rolling in order to obtain a fine lamellar ($\alpha + \beta$) microstructure. This microstructure leads to equiaxed primary α -grains and a comparable (compared to other studied processing routes not covered by the present study) small amount of retained lamellae after final deformation and recrystallization. The thicker plate of Ti-0.44O-0.5Fe-0.08C-0.4Si-0.1Au with a plate thickness of approx. 12 mm, however, did not exhibit martensite on the entire cross section, which resulted in a higher amount of residual lamellae after recrystallization annealing and lower mechanical properties. In terms of Ti-0.63O-0.58Fe-0.096C-2.10Mo, the microstructure is much finer and exhibits more β -phase than Ti-0.44O-0.5Fe-0.08C-0.4Si-0.1Au. However, the amount of retained lamellae is comparable high, but much less compared to other studied processing routes for this alloy.
- In terms of Ti-0.44O-0.5Fe-0.08C-0.4Si-0.1Au, rotary swaged and recrystallized material as well as the thinner plate, which was processed, exhibit a yield and ultimate tensile strength which are (almost) within typical values of Ti-6Al-4V in combination with a ductility of more than

18%. During fatigue tests of rotary swaged and recrystallized material, two specimens withstood a stress amplitude of approx. 248 MPa ($R \approx 0.02$) and of approx. 266 MPa ($R \approx 0.04$) without failure (5×10^6 cycles). This indicates that Ti-0.44O-0.5Fe-0.08C-0.4Si-0.1Au has a higher fatigue endurance limit than Ti-6Al-4V ELI, but further investigations are necessary, since only five specimens could be tested.

- Ti-0.63O-0.58Fe-0.096C-2.10Mo exhibits a very high yield and ultimate tensile strength of more than 1100 MPa, which are in the upper range of Ti-6Al-4V, and a ductility of more than 16%.
- Fracture surface analysis of the fatigue sample of Ti-0.44O-0.5Fe-0.08C-0.4Si-0.1Au suggests that hydrogen may play a role during fatigue crack initiation or propagation. Additionally, the comparable high oxygen content of this alloy might have a potential negative effect.

The present results indicate that Ti-0.44O-0.5Fe-0.08C-0.4Si-0.1Au and Ti-0.63O-0.58Fe-0.096C-2.10Mo are promising alternatives for Ti-6Al-4V for use in medical applications. However, further investigations are necessary, on the one hand, to study the fatigue properties of Ti-0.63O-0.58Fe-0.096C-2.10Mo. Since both alloys are intended for use in implant or osteosynthesis applications, on the other hand, the influence of corrosive environments on fatigue and tensile properties of both alloys and the role of hydrogen and oxygen on mechanical properties have to be investigated, since continued corrosive attacks will take place in the human body.

Materials and methods

Alloy production

In terms of Ti-0.44O-0.5Fe-0.08C-0.4Si-0.1Au, approx. 28 kg of this alloy were weighed out using CP-Titanium Grade 2 standard material (Ti-0.135O-0.05Fe-0.018C), CP-Titanium Grade 1 foil, TiO₂ powder (purity: 99.5%), graphite powder (99.9+%), gold granules (99.99%), iron chunks (99.98%), and silicon pieces (99.98%). The titanium foil was used to fold a bag, which contained all weighed out powder during melting. Alloy production was carried out at VACUCAST Feinguss GmbH & Co. Metall KG in Berlin, Germany, via cold crucible induction melting. After skull production, two smelting processes had been performed, after which bars with a diameter of approx. 38 mm and a length of approx. 360 mm were cast. These bars were further processed by VACUCAST before performing thermo-mechanical treatments and microstructure analyses.

In terms of Ti-0.44O-0.5Fe-0.08C-2.0Mo, approx. 36 kg of this alloy were produced at GfE Metalle und Materialien GmbH in Nürnberg, Germany. The ingot had a diameter of approx. 115 mm and a length of approx. 700 mm. The resulting chemical

composition was Ti-0.63O-0.58Fe-0.096C-2.10Mo according to the provided acceptance test certificate 3.1.

Thermo-mechanical processing

Comprehensive thermo-mechanical processing studies with varying experimental parameters had been performed preliminary on Ti-0.44O-0.5Fe-0.08C-0.4Si-0.1Au as well as Ti-0.44O-0.5Fe-0.08C-2.0Mo. These are not covered by the present study, but led to the optimized, multi-stage processing routes for plate rolling of Ti-0.44O-0.5Fe-0.08C-0.4Si-0.1Au and Ti-0.63O-0.58Fe-0.096C-2.10Mo, which are described in the following. The experimental parameters cited are those which were used to gain the experimental results described in this study. Both routes are very similar and only differ in temperature during solution annealing.

In a first step, cylindrical cuts with a diameter of approx. 38–40 mm and a length of e. g. 86 mm in terms of the silicon containing alloy and a rectangular cut of approx. 65 × 31 × 36 mm in terms of the molybdenum containing alloy were prepared for better handling with the laboratory-size two-high rolling mill (non-reversing). Prior to annealing and rolling, a paste based on ZrO₂, polyethylene glycol 400, and ethanol was applied as thermal barrier coating. In a second step, those cuts were annealed at 950°C for 45–49 min using a standard chamber furnace and subsequently rolled in several passes in order to produce a plate-type wrought product. Between individual passes resulting in a thickness reduction of usually 2 mm, the plates were annealed at 950°C for 10 min to ensure deformability. This rolling was not intended to introduce work hardening for microstructure recrystallization, but to gain a plate-like specimen. In a third step, the plates were subjected to a two-step annealing treatment, in which a fully martensite decomposition was used to gain a fine lamellar ($\alpha + \beta$) microstructure. For this purpose, first, the plates were solution treated near β -transus at approx. 1025°C (Ti-0.44O-0.5Fe-0.08C-0.4Si-0.1Au) or 1060°C (Ti-0.63O-0.58Fe-0.096C-2.10Mo) with subsequent water quenching to achieve a martensitic microstructure. The holding time was varied to take different plate thicknesses into account. In terms of the molybdenum containing alloy (plate thickness of approx. 12 mm), a holding time of 20 min was used. In terms of the silicon containing alloy, the holding times were chosen to be 10 min and 15 min for a plate thickness of approx. 8 mm and 12 mm, respectively. In terms of both plates with 12 mm thickness, the thermal barrier coating had been removed prior to solution annealing. However, in terms of Ti-0.44O-0.5Fe-0.08C-0.4Si-0.1Au, the cooling rate during water quenching of the thicker plate was, in contrast to the thinner plate, (still) not high enough to obtain a full martensitic microstructure. During the second step of the two-step annealing treatment, the plates were annealed at 900°C for 1.5 h with subsequent air

cooling. In the fourth step of the processing route, final rolling was conducted. First, a thermal barrier coating as described earlier had been applied, after which the plates were annealed at approx. 300°C for 20 min and 30 min in terms of the thinner and thicker plates, respectively. Rolling was conducted in several individual passes with a thickness reduction of approx. 0.2 mm in each step to achieve a final degree of deformation (in terms of plate thickness) of approx. 0.71 (thinner plate, silicon containing alloy), 0.80 (thicker plate, silicon containing alloy), and 0.75 (molybdenum containing alloy). Between each rolling step, the plates were annealed at approx. 300°C for 4–5 min. Recrystallization annealing was performed at 800°C for 2 h with subsequent air cooling to obtain an equiaxed microstructure.

Additionally, bars of Ti–0.44O–0.5Fe–0.08C–0.4Si–0.1Au were rotary swaged at the Institute for Production Engineering and Forming Machines (PtU) at Technical University of Darmstadt, Germany. First, they had been rotary swaged to a diameter of 18.4 mm in several steps, after which a further reduction to a final diameter of approx. 15 mm was performed resulting in a degree of deformation of approx. 0.41 during this last step. During deformation of bars with diameter below 20 mm, the deformation temperature was between 750 and 800°C. Afterward, the same recrystallization treatment (800°C for 2 h with air cooling) was applied as in terms of the rolled plates.

Microstructure analysis

For metallographic sample preparation, small samples were cut off, warm embedded into EpoMet™ G (used around specimen surface) and Bakelite (used as filler material) molding compound, and were subsequently ground, polished, and etched. Longitudinal sections were either cut or ground down to the approximate middle of the plate prior to grinding. Grinding was performed using SiC-grinding paper of grit sizes P180, P240, P320, P400, P600, P800, P1200, and P2500 with a pressure of 6 N (P1200 and P2500) or 10 N per specimen and with a rate of rotation of 150 min⁻¹ (counter rotation) in terms of the sample holder and the working wheel. Polishing was conducted with a polishing suspension containing SiO₂ particles of size 0.05 μm and H₂O₂ in a volume ratio of 5:1 using a force of 7 N per specimen and a rate of rotation of 80 min⁻¹ and 150 min⁻¹ (counter rotation) in terms of the sample holder and the working wheel, respectively. Etching was performed with different etchants and etching times depending on alloy and microstructure. In terms of Ti–0.44O–0.5Fe–0.08C–0.4Si–0.1Au, specimens were etched for approx 20 s with an etchant consisting of 86 ml H₂O, 4.5 ml HNO₃, 12 ml H₂O₂, and 5 ml HF. In terms of Ti–0.63O–0.58Fe–0.096C–2.10Mo, Kroll's reagent (100 ml H₂O, 6 ml HNO₃, 3 ml HF) was used for 5–10 s depending on microstructure.

For microstructure analysis, a ZEISS Axio Imager.M2m reflected light microscope (bright field mode with, if necessary, C-DIC method [27]) and, for higher magnification and local EDS analysis, a Hitachi TM3000 tabletop microscope (scanning electron microscope) provided with a BSE detector and a QUANTAX 70 EDS system from Bruker Nano operated with an acceleration voltage of 15 kV were used.

Mechanical properties

Tensile tests were performed at room temperature according to DIN EN ISO 6892-1:2017-02 [28] part B on rolled and recrystallized plates as well as on rotary swaged and recrystallized material. In terms of Ti–0.63O–0.58Fe–0.096C–2.10Mo, four flat tensile specimens (rolled and recrystallized material) were tested. The corresponding plate had a thickness of approx. 12 mm prior to solution annealing (see multi-stage processing route for plate rolling). In terms of rolled material of Ti–0.44O–0.5Fe–0.08C–0.4Si–0.1Au, tensile specimens were manufactured out of two different plates in order to determine the influence of different amounts of retained lamellae after recrystallization treatment on the resulting mechanical properties. The first plate (four specimens) had a thickness or approx. 8 mm and the second plate (two specimens) a thickness of approx. 12 mm prior to solution annealing. In all cases, flat tensile specimens according to DIN EN ISO 6892-1:2017-02 [28] were used with the testing direction parallel to the long axes of the rolled and recrystallized plates. In terms of rotary swaged and recrystallized material of Ti–0.44O–0.5Fe–0.08C–0.4Si–0.1Au, two round tensile specimens of type B4x20 according to DIN 50125:2016-12 [29] were used. During all tensile tests, the initial stress, the stress rate in the elastic regime, and the test speed was set to 5 MPa, 10 MPa/s, and 0.005 1/s or 0.006 1/s, respectively. A hysteresis loop was used for determination of the elastic modulus in order to get a better estimation of the yield strength. This yield strength was determined as strength at a plastic deformation of 0.2%. All tensile tests were performed on a universal testing machine (200 kN) with SCHENCK-TREBEL test frame and ZwickRoell ZMART.PRO control system.

Moreover, force-controlled fatigue tests were performed on rotary swaged and recrystallized material of Ti–0.44O–0.5Fe–0.08C–0.4Si–0.1Au. Five round specimens in the style of ASTM E466-15 [30] (specimens with tangentially blending filets between the test section and the ends) were manufactured. However, the diameter of the specimens in terms of the test section varied between approx. 3.4–4.0 mm. All specimens had a metric fine thread (M9) and, after machining, were first ground manually in radial direction with SiC-grinding paper up to a grit size of P2500 in order to remove any remaining scratches. Additional grinding was subsequently performed in longitudinal direction with a grit size of P2500 until no radial score marks were visible

in a stereomicroscope using ten times magnification. After measuring the diameter, all samples were, again, ground slightly with P2500 grinding paper in longitudinal direction to remove any scratches caused by the caliper. Finally, all specimens were cleaned in ethanol using an ultrasonic bath and any remaining scratches or abnormalities were documented. All fatigue tests were performed on a universal testing machine (100 kN) with SCHENCK test frame, INSTRON control system, and Wave-Matrix™ software. A sinusoidal force with a frequency of 8 Hz and a R-value between approx. 0.02 and 0.04 was used. Tests were performed at stress amplitudes/mean stresses of approx. 298/312, 270/285, 247/260, 248/259, 266/289 MPa and were stopped after 5×10^6 cycles. Since the duration of the transient response or the settling time of the testing machine was not constant for all specimens and took between a few ten thousand up to roughly 500,000 cycles, the stresses given are calculated as medium stresses after the transient response ended and were rounded to integers. During settling time, the maximum stress decreased and the minimum stress increased, which, therefore, has a negative impact on fatigue properties. However, it has to be noted that the ambient temperatures might not have satisfied room temperature and the air moisture might have changed throughout the tests.

After tensile and fatigue tests, fracture surface analysis was performed via scanning electron microscopy to study the microscopic fracture behavior. In terms of tensile tests, all specimens of Ti–0.44O–0.5Fe–0.08C–0.4Si–0.1Au and exemplary one specimen of Ti–0.63O–0.58Fe–0.096C–2.10Mo with lowest measured elongation after fracture were analyzed. In terms of fatigue tests, the specimen tested at the highest stress amplitude/medium stress of approx. 298/312 MPa and one specimen tested at the lowest stress level, but which fractured unsuspected early, were investigated. In all cases, a ZEISS LEO 1550 FE-SEM with an acceleration voltage of 5 kV and an Everhart-Thornley-Detector (SE-mode) was used.

Acknowledgments

The present study was performed as part of the project IGF 19708 N of the AiF Arbeitsgemeinschaft industrieller Forschungsvereinigungen “Otto von Guericke” e.V. Funding of this project by the Federal Ministry for Economic Affairs and Climate Action on the basis of a resolution of the German Bundestag is gratefully acknowledged. For smelting and casting of bars of Ti–0.44O–0.5Fe–0.08C–0.4Si–0.1Au, the authors would like to thank T. Sahin and S. Voigt from VACUCAST Feinguss GmbH & Co. Metall KG in Berlin, Germany. Moreover, the authors would like to thank H. Meißner, F. Graef, J. Weber, and T. Hamann of the Technische Universität Braunschweig for their assistance.

Funding

Open Access funding enabled and organized by Projekt DEAL. This research was conducted as part of project IGF 19708 N of the AiF Arbeitsgemeinschaft industrieller Forschungsvereinigungen “Otto von Guericke” e.V. This project is funded by the Federal Ministry for Economic Affairs and Climate Action on the basis of a resolution of the German Bundestag.

Data availability

The datasets generated during and/or analyzed during the current study are available from the corresponding author on reasonable request.

Code availability

Not applicable.

Declarations

Conflict of interest All authors have no competing interests to declare that are relevant to the content of this article.

Open Access

This article is licensed under a Creative Commons Attribution 4.0 International License, which permits use, sharing, adaptation, distribution and reproduction in any medium or format, as long as you give appropriate credit to the original author(s) and the source, provide a link to the Creative Commons licence, and indicate if changes were made. The images or other third party material in this article are included in the article's Creative Commons licence, unless indicated otherwise in a credit line to the material. If material is not included in the article's Creative Commons licence and your intended use is not permitted by statutory regulation or exceeds the permitted use, you will need to obtain permission directly from the copyright holder. To view a copy of this licence, visit <http://creativecommons.org/licenses/by/4.0/>.

References

1. L.-C. Zhang, L.-Y. Chen, A Review on biomedical titanium alloys: recent progress and prospect. *Adv. Eng. Mater.* **21**(4), 1801215 (2019). <https://doi.org/10.1002/adem.201801215>
2. Y. Li, C. Yang, H. Zhao, S. Qu, X. Li, Y. Li, New developments of Ti-based alloys for biomedical applications. *Materials* **7**(3), 1709–1800 (2014). <https://doi.org/10.3390/ma7031709>
3. M. Kawahara, M. Kato-Negishi, Link between aluminum and the pathogenesis of Alzheimer's disease: the integration of the

- aluminum and amyloid cascade hypotheses. *Int. J. Alzheimers Dis.* **2011**, 276393 (2011). <https://doi.org/10.4061/2011/276393>
4. D.R.C. McLachlan, P.N. Alexandrov, W.J. Walsh, A.I. Pogue, M.E. Percy, T.P.A. Kruck, Z. Fang, N. Scharfman, V. Jaber, Y. Zhao, W. Li, W.J. Lukiw, Aluminum in neurological disease—a 36 year multicenter study. *J. Alzheimers Dis. Parkinsonism* **8**(6), 457 (2018). <https://doi.org/10.4172/2161-0460.1000457>
 5. T. Tietz, A. Lenzner, A.E. Kolbaum, S. Zellmer, C. Riebeling, R. Gürtler, C. Jung, O. Kappenstein, J. Tentschert, M. Giubudagian, S. Merkel, R. Pirow, O. Lindtner, T. Tralau, B. Schäfer, P. Laux, M. Greiner, A. Lampen, A. Luch, R. Wittkowski, A. Hensel, Aggregated aluminium exposure: risk assessment for the general population. *Arch. Toxicol.* **93**(12), 3503–3521 (2019). <https://doi.org/10.1007/s00204-019-02599-z>
 6. K. Klotz, W. Weistenhöfer, F. Neff, A. Hartwig, C. van Thriel, H. Drexler, The health effects of aluminum exposure. *Dtsch. Arztebl. Int.* **114**(39), 653–659 (2017). <https://doi.org/10.3238/arztebl.2017.0653>
 7. D. Krewski, R.A. Yokel, E. Nieboer, D. Borchelt, J. Cohen, J. Harry, S. Kacew, J. Lindsay, A.M. Mahfouz, V. Rondeau, Human health risk assessment for aluminium, aluminium oxide, and aluminium hydroxide. *J. Toxicol. Environ. Health B Crit. Rev.* **10**(Suppl 1), 1–269 (2007). <https://doi.org/10.1080/10937400701597766>
 8. F. Haase, C. Siemers, L. Klinge, C. Lu, P. Lang, S. Lederer, T. König, J. Rösler, Aluminum- and vanadium-free titanium alloys for medical applications. *MATEC Web Conf.* **321**, 05008 (2020). <https://doi.org/10.1051/mateconf/202032105008>
 9. ASTM F67-13, *Standard Specification for Unalloyed Titanium, for Surgical Implant Applications (UNS R50250, UNS R50400, UNS R50550, UNS R50700)*. ASTM International, West Conshohocken, PA (2013). <https://doi.org/10.1520/F0067-13>
 10. C. Siemers, F. Brunke, K. Saksl, J. Kiese, M. Kohnke, F. Haase, M. Schlemminger, P. Eschenbacher, J. Fürste, D. Wolter, H. Sibus, Development of advanced titanium alloys for aerospace, medical and automotive applications, in *Proceedings of the XXVIII International Mineral Processing Congress (IMPC 2016), September 11-15 2016, Québec City, Canada* (Canadian Institute of Mining Metallurgy & Petroleum (CIM), Westmount, Canada, 2016), pp. 3600–3611
 11. C. Siemers, M. Bäker, F. Brunke, D. Wolter, H. Sibus, Aluminum- and vanadium-free titanium alloys for application in medical engineering, in *Titanium in Medical and Dental Applications*, ed. by F.H. Froes, M. Qian (Woodhead Publishing, Duxford, 2018), pp. 477–492. <https://doi.org/10.1016/B978-0-12-812456-7.00021-4>
 12. M.A. Zoroddu, J. Aaseth, G. Crisponi, S. Medici, M. Peana, V.M. Nurchi, The essential metals for humans: a brief overview. *J. Inorg. Biochem.* **195**, 120–129 (2019). <https://doi.org/10.1016/j.jinorgbio.2019.03.013>
 13. G. Lütjering, J.C. Williams, *Titanium*, 2nd edn. (Springer, Berlin, 2007). <https://doi.org/10.1007/978-3-540-73036-1>
 14. M. Akhtar, A. Khajuria, J.K. Sahu, J. Swaminathan, R. Kumar, R. Bedi, S.K. Albert, Phase transformations and numerical modelling in simulated HAZ of nanostructured P91B steel for high temperature applications. *Appl. Nanosci.* **8**(7), 1669–1685 (2018). <https://doi.org/10.1007/s13204-018-0854-1>
 15. A. Khajuria, M. Akhtar, R. Bedi, A novel approach to envisage effects of boron in P91 steels through Gleeble weld-HAZ simulation and impression-creep. *J. Strain Anal. Eng. Des.* (2021). <https://doi.org/10.1177/03093247211061943>
 16. Y. Iijima, S.-Y. Lee, K.-I. Hirano, Diffusion of silicon, germanium and tin in β -titanium. *Philos. Mag. A* **68**(5), 901–914 (1993). <https://doi.org/10.1080/01418619308219375>
 17. H. Nakajima, M. Koiwa, Diffusion in titanium. *ISIJ Int.* **31**(8), 757–766 (1991). <https://doi.org/10.2355/isijinternational.31.757>
 18. DIN Deutsches Institut für Normung e.V., *DIN EN ISO 5832-3:2017-03, Implants for surgery—Metallic materials—Part 3: Wrought titanium 6-aluminium 4-vanadium alloy (ISO 5832-3:2016); German version EN ISO 5832-3:2016*. Beuth Verlag GmbH, Berlin. <https://doi.org/10.31030/2506055>
 19. M. Peters, J. Hemptenmacher, J. Kumpfert, C. Leyens, Structure and properties of titanium and titanium alloys, in *Titanium and Titanium Alloys: Fundamentals and Applications*, ed. by C. Leyens, M. Peters (Wiley, Weinheim, 2003), pp. 1–36. <https://doi.org/10.1002/3527602119.ch1>
 20. Y. Ono, T. Yuri, T. Ogata, S. Matsuoka, H. Sunakawa, Effect of stress ratio on high-cycle fatigue properties of Ti-6Al-4V ELI alloy forging at low temperature. *AIP Conf. Proc.* **1574**, 23–26 (2014). <https://doi.org/10.1063/1.4860599>
 21. G. Lange, Mikroskopische und makroskopische Erscheinungsformen des duktilen Gewaltbruches (Gleitbruch), in *Systematische Beurteilung technischer Schadensfälle*, 6th edn., ed. by G. Lange, M. Pohl (Wiley, Weinheim, 2014), pp. 79–102. <https://doi.org/10.1002/9783527683161.ch5>
 22. A.L. Pilchak, J.C. Williams, Observations of Facet formation in near- α titanium and comments on the role of hydrogen. *Metall. Mater. Trans. A* **42**(4), 1000–1027 (2011). <https://doi.org/10.1007/s11661-010-0507-9>
 23. H. Müller, A. Ibach, Makroskopische und mikroskopische Erscheinungsformen des Spaltbruches, in *Systematische Beurteilung technischer Schadensfälle*, 6th edn., ed. by G. Lange, M. Pohl (Wiley, Weinheim, 2014), pp. 103–126. <https://doi.org/10.1002/9783527683161.ch6>
 24. G. Lange, Makroskopisches und mikroskopisches Erscheinungsbild des Schwingbruches, in *Systematische Beurteilung technischer Schadensfälle*, 6th edn., ed. by G. Lange, M. Pohl (Wiley, Weinheim, 2014), pp. 127–220. <https://doi.org/10.1002/9783527683161.ch7>

25. M. Peters, A. Gysler, G. Lütjering, Influence of texture on fatigue properties of Ti–6Al–4V. *Metall. Mater. Trans. A* **15**(8), 1597–1605 (1984). <https://doi.org/10.1007/BF02657799>
26. A. Amherd Hidalgo, T. Ebel, W. Limberg, F. Pyczak, Influence of oxygen on the fatigue behaviour of Ti–6Al–7Nb alloy. *Key Eng. Mater.* **704**, 44–52 (2016). <https://doi.org/10.4028/www.scientific.net/KEM.704.44>
27. R. Danz, P. Gretscher, C-DIC: a new microscopy method for rational study of phase structures in incident light arrangement. *Thin Solid Films* **462–463**, 257–262 (2004). <https://doi.org/10.1016/j.tsf.2004.05.124>
28. DIN Deutsches Institut für Normung e.V., DIN EN ISO 6892-1:2017-02, *Metallic Materials—Tensile Testing—Part 1: Method of Test at Room Temperature (ISO 6892-1:2016)*; German version EN ISO 6892-1:2016 (Beuth Verlag GmbH, Berlin). <https://doi.org/10.31030/2384831>
29. DIN Deutsches Institut für Normung e.V., DIN 50125:2016-12, *Testing of Metallic Materials—Tensile Test Pieces* (Beuth Verlag GmbH, Berlin). <https://doi.org/10.31030/2577390>
30. ASTM E466-15, *Standard Practice for Conducting Force Controlled Constant Amplitude Axial Fatigue Tests of Metallic Materials* (ASTM International, West Conshohocken, PA). <https://doi.org/10.1520/E0466-15>